Received: 5 April 2019 | Revised: 23 August 2019 | Accepted: 23 August 2019

DOI: 10.1002/mrm.27994

FULL PAPER

Magnetic Resonance in Medicine

Spiral blurring correction with water–fat separation for magnetic resonance fingerprinting in the breast

Teresa Nolte[1] | **Nicolas Gross-Weege**[1] | **Mariya Doneva**[2] | **Peter Koken**[2] | **Aaldert Elevelt**[3] | **Daniel Truhn**[4] | **Christiane Kuhl**[4] | **Volkmar Schulz**[1]

[1]Physics of Molecular Imaging Systems, Experimental Molecular Imaging, RWTH Aachen University, Aachen, Germany

[2]Tomographic Imaging Systems, Philips Research Europe, Hamburg, Germany

[3]Oncology Solutions, Philips Research Europe, Eindhoven, The Netherlands

[4]Clinic for Diagnostic and Interventional Radiology, University Hospital Aachen, Aachen, Germany

Correspondence
Volkmar Schulz, Center for Biohybrid Medical Systems, Forckenbeckstr. 55, 52074 Aachen, Germany.
Email: volkmar.schulz@pmi.rwth-aachen.de

Funding information
European Union's Horizon 2020 research and innovation programme under the Marie Skłodowska-Curie grant, Grant/Award Numbers: 642445 and 667211

Purpose: Magnetic resonance fingerprinting (MRF) with spiral readout enables rapid quantification of tissue relaxation times. However, it is prone to blurring because of off-resonance effects. Hence, fat blurring into adjacent regions might prevent identification of small tumors by their quantitative T_1 and T_2 values. This study aims to correct for the blurring artifacts, thereby enabling fast quantitative mapping in the female breast.

Methods: The impact of fat blurring on spiral MRF results was first assessed by simulations. Then, MRF was combined with 3-point Dixon water–fat separation and spiral blurring correction based on conjugate phase reconstruction. The approach was assessed in phantom experiments and compared to Cartesian reference measurements, namely inversion recovery (IR), multi-echo spin echo (MESE), and Cartesian MRF, by normalized root-mean-square error (NRMSE) and SD calculations. Feasibility is further demonstrated in vivo for quantitative breast measurements of 6 healthy female volunteers, age range 24–31 y.

Results: In the phantom experiment, the blurring correction reduced the NRMSE per phantom vial on average from 16% to 8% for T_1 and from 18% to 11% for T_2 when comparing spiral MRF to IR/MESE sequences. When comparing to Cartesian MRF, the NRMSE reduced from 15% to 8% for T_1 and from 12% to 7% for T_2. Furthermore, SDs decreased. In vivo, the blurring correction removed fat bias on T_1/T_2 from a rim of ~7–8 mm width adjacent to fatty structures.

Conclusion: The blurring correction for spiral MRF yields improved quantitative maps in the presence of water and fat.

KEYWORDS
blurring correction, breast imaging, fat bias, fat water blurring, magnetic resonance fingerprinting, quantitative MRI

This is an open access article under the terms of the Creative Commons Attribution License, which permits use, distribution and reproduction in any medium, provided the original work is properly cited.
© 2019 The Authors. *Magnetic Resonance in Medicine* published by Wiley Periodicals, Inc. on behalf of International Society for Magnetic Resonance in Medicine

1 | INTRODUCTION

Quantitative magnetic resonance imaging (qMRI) offers a vendor-independent imaging contrast, which promises the identification and classification of lesions based on their intrinsic tissue properties.[1,2] Moreover, quantitative image data represents an ideal input for post processing, such as machine learning methods.[3] The tissue relaxation times T_1 and T_2 are intrinsic tissue parameters that underlie the contrast formation of the clinically used qualitative (i.e., contrast-weighted) MR images. However, the acquisition of quantitative parameter maps has not yet widely found its way into clinical practice, mainly because of long scan times.

In breast imaging, previous reports suggest that qMRI can help to determine the response to neoadjuvant chemotherapy[4-6] (namely, decreased T_2 values are reported for responders) as well as to distinguish invasive ductal carcinoma from healthy tissue[7] or between different types of lesions.[8,9] Moreover, if the corresponding relaxation times prove to differ significantly, a fast quantitative breast imaging protocol may be of interest in contrast-agent free breast screening.

Magnetic resonance fingerprinting (MRF) is a fast sequence that measures several quantitative markers at a time[10,11] from an image series with varying acquisition parameters such as flip angles, TRs, and RF phases. The measured signal evolution in every voxel is compared to a dictionary of simulated signal evolutions, which permits to select the best-matching quantitative parameters. MRF allows for highly efficient parameter estimation, as the MRF signal is acquired during transient state while making use of high undersampling during readout in each TR interval. For long enough MRF sequences, correct identification of the underlying tissue properties is possible as long as the resulting undersampling artifacts distribute in a noise-like manner around the true signal evolution.[11-13] Spiral readout is often preferred for MRF because of its sampling speed and large k-space coverage.[14]

However, spiral sampling results in blurred images for off-resonant spins. This effect becomes especially important if the FOV does not only contain aqueous tissues, but also fat, of which the main spectral peak presents an average chemical shift of ~−3.5 ppm with respect to the resonance frequency of water.[15] In consequence, fat signal that has blurred into adjacent voxels may obscure the contours of tissues as well as the presence of adjacent structures of interest, such as small tumors. A conjugate phase reconstruction (CPR) allows correction for off-resonance induced blurring artefacts in spiral images.[16] Yet, CPR requires knowledge about the spatial off-resonance distribution. A different approach that circumvents fat blurring is suppression of the fat signal (e.g., by fat saturation techniques).[17] Fat-saturated MRF was recently presented in the abdomen as well as in female breast.[7,18] However, fat saturation techniques may not always yield complete suppression of the fat signal over the entire FOV, especially at higher field strengths and/or in breast MRI protocols that involve larger FOVs to cover both breasts such as the axial bilateral imaging protocols used for breast cancer screening. In the female breast anatomy, the fat signal may provide diagnostic information as well. For instance, keeping the fat signal in T_2-weighted images permitted the distinction of benign from malignant tumors in such lesions that showed enhancement during dynamic contrast enhanced MRI.[19]

In this work, we extend MRF by a Dixon water–fat separation approach,[20] which allows to correct for the fat blurring. The presented method does not require the separate acquisition of an off-resonance map. It is inspired by the approach of Boernert et al,[21] who combined a 3-point Dixon method with CPR on fully sampled spiral images. CPR can equally deblur undersampled MRF data.[22,23] In both cases, the authors characterized the off-resonance map in a separate scan before computing the CPR of the individual, undersampled images. Preliminary results on fat blurring-corrected MRF with water–fat separation were recently presented.[24,25] Very recently, alternative MRF methods estimating water T_1 and T_2/water T_1 and fat T_1 as well as the fat signal fraction were proposed.[26,27] However, the breast anatomy has not yet been addressed.

We therefore propose 2D blurring-corrected MRF with Dixon water–fat separation in the female breast, where both aqueous fibroglandular tissue as well as fatty tissue are present. Thereby, quantitative parameter maps of the relaxation times in the breast as well as the off-resonance map are obtained.

2 | METHODS

2.1 | CPR for spiral off-resonance blurring correction

Spiral MRI is prone to off-resonance artifacts. Deviations $\Delta\omega$ from the water proton resonance frequency ω_0 may result from the background inhomogeneity of the main magnetic field (i.e., because of local differences in magnetic susceptibility) or from the chemical shift of a tissue, as in the case of fat. If a spin distribution $\rho(\boldsymbol{r})$ is subject to any type of spatially varying off-resonance frequency $\Delta\omega(\boldsymbol{r})$, the MR signal can be written as

$$S(t) = \int \rho(\boldsymbol{r}) \exp(-i\Delta\omega(\boldsymbol{r})\, t) \exp(-i\boldsymbol{r}\Delta\boldsymbol{k}(t))\, d\boldsymbol{r}. \quad (1)$$

For reconstruction, the spiral signal $S(t)$ is commonly interpolated onto a Cartesian k-space grid before Fourier transformation into the image space[28] (i.e., both $\boldsymbol{r} = (x, y)$ and $\boldsymbol{k}(t) = \left(k_x(t), k_y(t)\right)$ are defined on a Cartesian grid). According to Equation 1, the true spin distribution $\rho(\boldsymbol{r})$ accrues an extra phase term during signal readout if $\Delta\omega(\boldsymbol{r}) \neq 0$. Therefore, standard image reconstruction by inverse Fourier

transform results in a blurred image $M(\boldsymbol{r}) = \mathcal{F}^{-1}(S(\boldsymbol{k}))$, as $\rho(\boldsymbol{r})$ is convolved by the spiral point spread function in the image space.[29] However, if the off-resonance map $\Delta\omega(\boldsymbol{r})$ as well as the spiral trajectory $\boldsymbol{k}(t)$ are known, the blurring-free $\rho(\boldsymbol{r})$ can be well approximated[16] by calculating the CPR

$$\rho^{CPR}(\boldsymbol{r}) = \frac{1}{(2\pi)^2} \int S(\boldsymbol{k}) \exp(i\Delta\omega(\boldsymbol{r})\tau(\boldsymbol{k})) \exp(i\boldsymbol{r}\cdot\boldsymbol{k})\, d\boldsymbol{k}. \quad (2)$$

Here, $\tau(\boldsymbol{k})$ is a map that indicates the time at which a k-space location is reached. Numeric implementation of the CPR comprises the following steps: (1) compute $\tau(\boldsymbol{k})$ from the gradient shapes, (2) transform the blurred image $M(\boldsymbol{r})$ into k-space, and (3) demodulate each pixel of location $\boldsymbol{r} = (x, y)$ at the corresponding off-resonance frequency $\Delta\omega(\boldsymbol{r})$. Step 3 can be accelerated by demodulating $S(\boldsymbol{k})$ with an array of discrete, evenly spaced off-resonance frequencies.[30] Here, an array of equidistant frequencies $\Delta\omega_i = 2\pi \cdot [-200, 200]$ rad/s is used to compute 201 demodulations of the blurry image. For each location $\boldsymbol{r}$, the deblurred pixel value is chosen from the image with the demodulation frequency $\Delta\omega_i$ that is closest to $\Delta\omega(\boldsymbol{r})$. Acceleration is important, knowing that MRF requires computing the CPR for a large series of images.

If both aqueous and fatty tissues are present in the FOV, they experience different $\Delta\omega$: a distribution of water protons $\rho^w(\boldsymbol{r})$ sees only the inhomogeneity of the main magnetic field: $\Delta\omega^w(\boldsymbol{r}) = \Delta\omega_0(\boldsymbol{r})$. In contrast, for a distribution of fat protons $\rho^f(\mathbf{r})$, the off-resonance frequency is shifted by −3.5 ppm: $\Delta\omega^f(\boldsymbol{r}) = \Delta\omega_0(\boldsymbol{r}) + \Delta\omega_{cs}$. At 1.5T, the chemical shift of fat with respect to water is $\Delta\omega_{cs} = -2\pi \cdot 220$ rad/s.

2.2 | MRF-Dixon with spiral deblurring

To correct for off-resonance blurring in MRF, we combined spiral MRF with 3-point Dixon water–fat separation and CPR deblurring. For superposing signal fractions of water and fat in the same voxel, the resulting voxel signal $M(\boldsymbol{r}) = M^w(\boldsymbol{r}) + M^f(\boldsymbol{r})$, acquired at TE, may be written as

$$\begin{aligned} M(\boldsymbol{r}) = &[\rho^w(\boldsymbol{r}) + \rho^f(\boldsymbol{r}) \exp(i\Delta\omega_{cs}\mathrm{TE})] \\ &\exp(i\Delta\omega_0(\boldsymbol{r})\mathrm{TE}) \exp(i\phi_0(\boldsymbol{r})). \end{aligned} \quad (3)$$

Here, ϕ_0 is a constant receiver offset-phase. For simplicity, we use a single peak fat model, although fat exhibits multiple spectral components. In three-point Dixon methods, 3 complex images $M_q(\boldsymbol{r})$ $(q = \{1, 2, 3\})$ of different echo times $\mathrm{TE_q}$ are acquired and serve to recover $\rho^w(\boldsymbol{r})$, $\rho^f(\boldsymbol{r})$, and $\Delta\omega_0(\boldsymbol{r})$. In our MRF-Dixon approach, we select $\mathrm{TE_q} = (2\pi/\Delta\omega_{cs}) + (\mathrm{q}-1)\,\Delta\mathrm{TE}$, with $\Delta\mathrm{TE} = \pi/\Delta\omega_{cs}$, which allows for an analytical solution of the water–fat separation.[15]

The MRF-Dixon acquisition and post-processing are sketched in Figure 1. The MRF sequence is a gradient-spoiled (i.e., unbalanced) gradient echo sequence using variable flip angles (FA) and constant TR. Three MRF trains of N pulses are played out, which are separated by a delay time Δt_d. Each MRF train is preceded by a 180° inversion pulse to enhance sensitivity to T_1.[31] Spiral acquisition begins after each RF excitation at $\mathrm{TE_q}$ for the q-th MRF train. In result, $3N$ undersampled complex images are acquired, with water and fat signal in-phase, out-of-phase, and in-phase again for the first, second, and third MRF train, respectively.

First, the off-resonance map is retrieved from the undersampled MRF data. Temporal averages over each of the 3 MRF trains are calculated, which highly reduces the undersampling induced aliasing artifacts that are present in the individual images

$$\bar{M}_q = \sum_{j=1}^{N} M_{qj}. \quad (4)$$

The mean off-resonance map

$$\overline{\Delta\omega_0} = \arg\left(\frac{\bar{M}_3}{\bar{M}_1}\right) / (2\Delta\mathrm{TE}), \quad (5)$$

is calculated and phase unwrapping is applied to $\overline{\Delta\omega_0}$ if phase jumps are present within the breast. Phase unwrapping was implemented as a region-growing algorithm.[15] The unwrapped off-resonance map is then used to execute a 3-point Dixon water–fat separation on every individual time point $j = 1 \ldots N$ of the MRF acquisition. Hence, a blurred water-only and a fat-only MRF train are retrieved. For the next post-processing step, a CPR with $\Delta\omega = \overline{\Delta\omega_0}$ is conducted on every complex image of the water-only MRF train, whereas a CPR with $\Delta\omega = \overline{\Delta\omega_0} + \Delta\omega_{cs}$ is conducted on every complex image of the fat-only MRF train. After CPR calculation, the deblurred water-only and fat-only data set are recombined (i.e., added up) and subsequently matched to an MRF dictionary of simulated signal evolutions.

2.3 | Experimental

2.3.1 | Simulation study: MRF with off-resonance blurring

We conducted simulation studies to estimate the impact of spiral off-resonance blurring on the MRF relaxation times of structures near fatty tissue in the breast. The simulation phantom (square of 224 × 224 voxels, FOV = 430 × 430 mm^2) contained a ring of fatty tissue and an adjacent small test structure (TS) (square of 5 × 5 voxels, distance of 1 voxel/1.92 mm to the fat border), both embedded in fibroglandular (FG) tissue. The nominal T_1 and T_2 maps in Figure 2A,B show the 100 × 100 voxel region containing

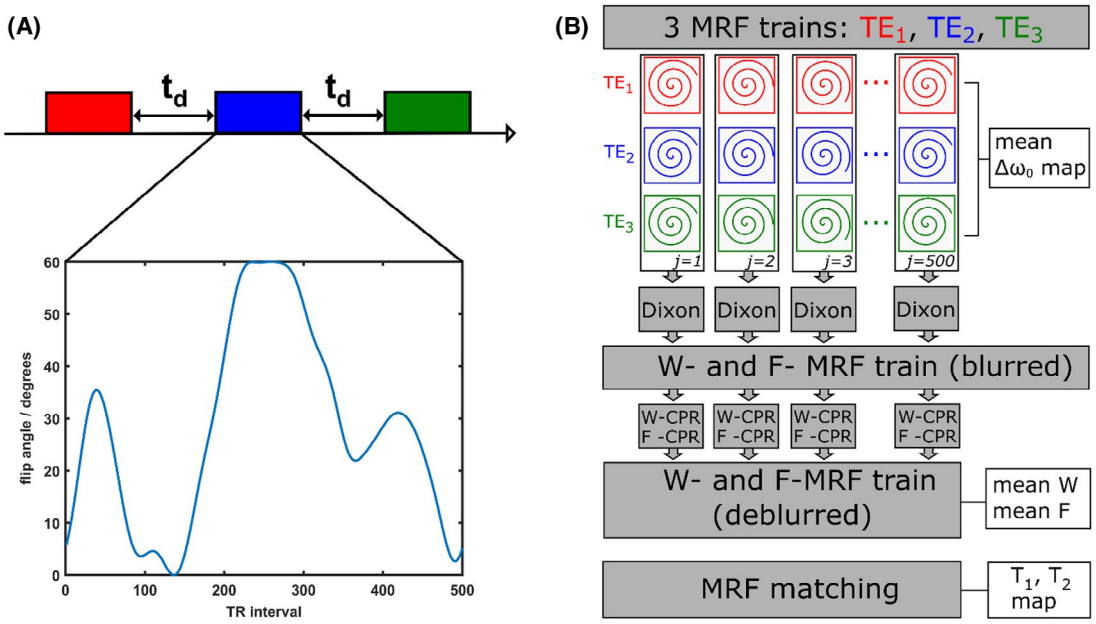

FIGURE 1 (A) MRF-Dixon acquisition. Three MRF trains of $j = 1 \ldots 500$ TR intervals each are acquired, differing in their TE. The flip angle trains are separated by a delay time t_d. The flip angle train with a length of 500 TR intervals is shown in the bottom left. It is preceded by a 180° inversion pulse and has previously been published by Sommer et al.[33] (B) MRF-Dixon post-processing scheme. As a first step, the mean off-resonance map is computed from the temporal averages of the in-phase MRF trains (TE_1, TE_3). With the mean off-resonance map, a 3-point Dixon water–fat separation is conducted for each TR interval. A blurred water MRF train and a blurred fat MRF train are obtained, which are subsequently deblurred by CPR. By calculating the temporal average over the deblurred water and fat MRF train, we obtain a mean water and a mean fat image. In a last step, the deblurred water and fat data are recombined and subjected to the MRF matching process. In result, deblurred T_1 and T_2 maps are obtained

the structures of interest. We simulated MRF signal evolutions of the 3 tissues as well as a full MRF dictionary based on the extended phase graph (EPG) formalism[32] using MATLAB (The MathWorks, Natick, MA). EPG simulations used the FA sequence[33] depicted in Figure 1A preceded by an 180° inversion pulse, an unbalanced gradient in slice selection direction, TR/TE = (20/4.6) ms. The T_1 and T_2 resolution of the dictionary was as stated in Table 1. In a first study, we assessed the impact of fat blurring because of chemical shift on the TS depending on the spiral acquisition time T_{acq}, setting $\Delta\omega = \Delta\omega_{cs}$ within the fatty tissue and $\Delta\omega = 0$ elsewhere. Hence, the fat signal was deliberately blurred using Equation 2 with $\Delta\omega = -\Delta\omega_{cs}$ and spiral k-space trajectories of different T_{acq}. After matching the blurred MRF data to the dictionary, we examined line profiles of T_1 and T_2 through the TS as well as the mean relaxation times and SDs within the TS. In a second study, we added different constant background off-resonance frequencies $\Delta\omega_0$ between 0 and $-150 \cdot 2\pi$ rad/s to the simulation ($\Delta\omega = \Delta\omega_0 + \Delta\omega_{cs}$ in fatty tissue, $\Delta\omega = \Delta\omega_0$ elsewhere, T_{acq} fixed to 7 ms). We also simulated off-resonance blurring alone ($\Delta\omega = \Delta\omega_0$ throughout all tissues), the situation corresponding to a center frequency blurring correction only (i.e., correcting only for the fat blurring because of chemical shift). Again, line profiles through the TS as well as mean relaxation times and SDs within the TS were examined.

In a third simulation study, we obtained MRF results for 2 spatially varying background off-resonance maps (i.e., for a linear and a parabolic background off-resonance field with $\Delta\omega_0$ varying between −200 and 0 Hz). Again, T_{acq} was fixed to 7 ms. As before, we simulated the combined effect of background off-resonance and fat blurring because of chemical shift as well as fat blurring because of chemical shift alone.

2.3.2 | Phantom validation

To validate the MRF-Dixon acquisition, a water–fat phantom containing 8 vials with mixtures of gelatin and varying amounts of a gadolinium (Gd)-based contrast agent embedded in lard was prepared and scanned next to a 1 L bottle of $CuSO_4$/water solution. MR scans were acquired on a 1.5T system (Achieva, Philips, Best, the Netherlands) with a 4-channel breast coil (Invivo, Gainesville, FL) in axial orientation. The performed scans and their durations are stated in Table 2. For MRF-Dixon scans, a square FOV of 430×430 mm^2 with voxel size of $(1.92 \times 1.92 \times 5)$ mm^3 was selected. As in the simulation study, we used a constant TR of 20 ms and the train of 500 flip angles[33] depicted in

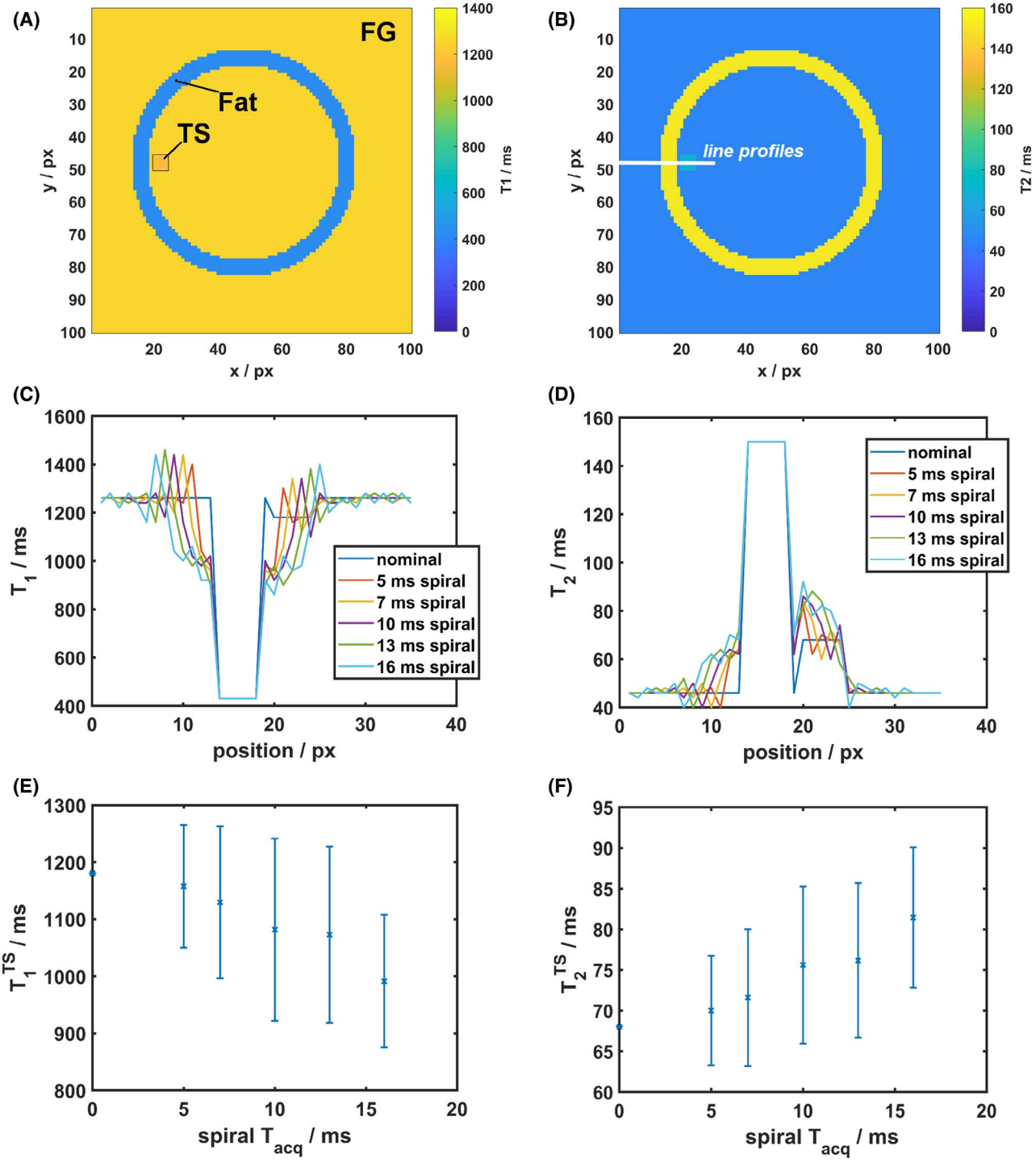

FIGURE 2 Simulation study of spiral blurring for a phantom containing fibroglandular tissue (FG), a small test structure (TS) of slightly different relaxation times, and a ring-shaped fatty structure. (A and B) Nominal MRF T_1 and T_2 maps without any spiral blurring. (C and D) Effect of fat blurring because of chemical shift, with the background off-resonance set to $\Delta\omega_0 = 0$ rad/s. Line profiles through the test structure are depicted for different spiral T_{acq} between 5 ms and 16 ms for T_1 and T_2. (E and F) Bias in mean T_1 and T_2 values within the TS caused by fat blurring because of chemical shift as well as the corresponding SD, calculated for the different spiral T_{acq}

Figure 1A, preceded by a 180° inversion pulse. Echo times ($TE_1/TE_2/TE_3 = 4.61/6.92/9.23$ ms) were set for the 3 MRF trains, corresponding to in-phase/out-of-phase/in-phase readout at 1.5T. The delay time in between the MRF trains was set to $t_d = 7.5$ s to allow for complete relaxation of the magnetization in breast tissues. A single spiral interleaf of uniform sampling density (acquisition window $T_{acq} = 7$ms) was acquired in each TR interval, corresponding to 20-fold undersampling or an acceleration factor of $R = 20$. Between successive TR intervals, the k-space trajectory was rotated by

TABLE 1 Parameter ranges and resolution of the MRF dictionary

Parameter	Range	Step size
T_1/ms	[5,200]	5
	[210,500]	10
	[520,2000]	20
T_2/ms	[2,100]	2
	[105,200]	5
	[210,500]	10
f_{B1+}	[0.7, 1.3]	0.025

Abbreviation: f_{B1+}, B1 correction factor.

TABLE 2 Scan durations for phantom and in vivo scans

Scan	Scan duration, phantom experiment	Scan duration, in vivo experiments
Spiral MRF-Dixon, US, $R = 20$	53 s	53 s
Spiral MRF-Dixon, FS, $R = 1$	–	17 min 31 s
Cartesian MRF	52 min 34 s	–
B_1 map (3D)	3 min 38 s	3 min 38 s
IR measurements	22 min 0 s	12 min 0 s
MESE measurements	30 min 20 s	9 min 6 s
Cartesian 3-point Dixon	3 min 17 s	3 min 17 s

Abbreviations: US, undersampled; FS, fully sampled; *R*, acceleration factor with respect to full sampling; IR, inversion recovery; MESE, multi-echo spin echo. Scans marked with "–" were not acquired.

18°. The transmit field (B_1^+) inhomogeneity over the slice was measured in a separate Cartesian 3D sequence using the actual flip angle technique.[34] The MRF-Dixon data set was deblurred based on the above-described approach. To compare between different sampling strategies, Cartesian MRF data was further acquired with TE = 4.61 ms. To retrieve T_1 and T_2 parameter maps, a dictionary with ~300,000 normalized entries was calculated. B_1^+ inhomogeneity was included in the dictionary as a multiplicative correction factor f_{B1+} in front of the flip angle train. The dictionary resolution is specified in Table 1. To reconstruct T_1 and T_2 maps, the measured signal evolution in every voxel was first normalized to a magnitude of 1 and then compared to the subset of dictionary entries with f_{B1+} closest to the measured B_1^+ of that voxel. The best matching dictionary entry was selected based on the maximum inner product between dictionary entry and measured signal evolution.[10] To evaluate the effect of CPR deblurring on the matching results, matching was equally performed to the first MRF-train M_1 without any correction for blurring, equal to the standard MRF measurement and matching procedure.[10]

All Cartesian reference scans were acquired with a reduced FOV of 80% in right-left direction to shorten the overall scan time. The readout bandwidth was maximized for the Cartesian scans, corresponding to an actual fat shift of 0.127 pixels (px). Quantitative Cartesian reference measurements (i.e., inversion recovery [IR] for T_1 and multi-echo spin echo [MESE] for T_2) were acquired and compared to the results of the MRF matching. IR measurements in the phantom used 11 inversion times TI = (50, 100, 200, 400, 600, 800, 1100, 1500, 2000, 3000, 5000), a turbo factor of 16 and TR/TE = (10,000/3.5) ms. T_1 values were retrieved for every voxel by fitting the function

$$M(\mathrm{TI}) = M_0 \left| 1 - 2\exp\left(-\frac{\mathrm{TI}}{\mathrm{T_1}}\right) + \exp\left(-\frac{\mathrm{TR}}{\mathrm{T_1}}\right)\right|, \quad (6)$$

to the time series of IR images. For the MESE sequence in the phantom, $n = 1 \ldots 30$ images with $\mathrm{TE_n} = n \cdot 35$ ms and TR = 10,000 ms were acquired. T_2 values were retrieved for every voxel by fitting the function

$$M(\mathrm{TE}) = M_0 \exp\left(-\frac{\mathrm{TE}}{\mathrm{T_2}}\right), \quad (7)$$

to the time series of MESE images. Circular regions of interest (ROI) covering the phantom vials were defined and means and SDs of T_1 and T_2 within each phantom vial were calculated. For each phantom vial, normalized root-mean-square errors (NRMSE) were calculated between the spiral MRF and the reference sequences

$$\mathrm{NRMSE}(A,B) = \sqrt{\sum_{j \in ROI} \frac{\mathrm{T_{ij}^A} - \mathrm{T_{ij}^B}}{\mathrm{T_{ij}^B}}}. \quad (8)$$

Here, $i = \{1, 2\}$. "A" stands for either the standard MRF or the MRF-Dixon measurement, while "B" stands for either the IR/MESE or the Cartesian MRF reference measurement.

2.3.3 | In vivo breast scans

Breast MR scans were acquired from 6 female healthy volunteers after informed consent, with age and ACR breast density as stated in Table 3. The breasts were immobilized in cranio–caudal direction.

As in the phantom, an undersampled spiral MRF-Dixon sequence was acquired ($R = 20$). To verify the robustness of our MRF-Dixon acquisition in vivo to undersampling artifacts and hence the quality of the parameter maps, a fully sampled MRF measurement ($R = 1$) was performed for 3 of the 6 volunteers. The MRF data sets were deblurred based on the above-described approach using CPR. For comparison purposes, some of the data were reconstructed a second time using a center frequency correction only.

TABLE 3 Age and ACR breast density of the volunteers

Volunteer	Age	ACR breast density
1	25	2
2	27	3
3	24	4
4	26	4
5	31	3
6	28	3

A Cartesian 3-point Dixon sequence was performed as a reference for water–fat separation and to validate our CPR deblurring correction. Echo times ($TE_1/TE_2/TE_3$ = 1.42/2.92/4.42) ms were used, thereby maximizing SNR with a phase accrual of 120° between successive echoes. TR was set to 1000 ms and the flip angle was set to 20°. The scanner software reconstructed images of the water and the fat signal as well as an off-resonance map, based on an iterative least squares approach[35] and a multi-peak spectral model of fat.

Reference IR measurements in the volunteers used 12 TI = (100, 200, 300, 400, 500, 600, 800, 1000, 1300, 1600, 2000, 2300 ms), a turbo factor of 10 and TR/TE = 3000/4.61 ms. For the T_2 reference measurement, $n = 1 \ldots 30$ images with $TE_n = n \cdot 9.22$ ms and TR = 3000 ms were acquired.

3 | RESULTS

3.1 | Simulation study

Figure 2 shows the simulations of fat blurring because of chemical shift. Figure 2A,B depict the nominal MRF T_1 and T_2 maps without any blurring. Line profiles through the TS with fat blurring are shown in Figure 2C,D. With increasing spiral T_{acq}, blurred fat signal smears out of the fatty tissue region. Already for short T_{acq}, fat signal shifts over the contour of the TS, thereby dissimulating it. For $T_{acq} = 7$ ms, which was also used for the measurements, blurred fat signal spreads over ~4 pixels (i.e., ~7–8 mm). With increasing T_{acq}, the quantitative T_1 and T_2 values in the TS become increasingly biased toward the fat relaxation times. Moreover, the fat blurring adds variability to the values. These 2 effects become equally visible in Figure 2E,F, depicting mean values and SDs of T_1 and T_2 within the TS against T_{acq}. Supporting Information Figure S1 shows the simulations with additional background off-resonance blurring. With both background off-resonance blurring and fat blurring because of chemical shift, the line profiles in Supporting Information Figure S1A,B show heavy distortions for all $\Delta\omega_0$, because all tissues blur into neighboring areas. This is reflected by broad distributions of T_1 and T_2 values over the TS and therefore large SDs (cf. Supporting Information Figure S1C,D). Supporting Information Figure S1E,F show that background off-resonance blurring alone already mildly distorts the line profiles at $\Delta\omega_0 = -25 \cdot 2\pi$ rad/s, with increasing effect toward stronger background off-resonances. This results in increasing bias and variability on the mean relaxation times in the TS (c.f. Supporting Information Figure S1G,H). Supporting Information Figure S2 shows the third simulation study, which included spatially varying background off-resonance maps. Supporting Information Figure S2A shows MRF T_1 and T_2 maps simulated for the linearly varying $\Delta\omega_0$ map, while Supporting Information Figure S2B shows MRF T_1 and T_2 maps for the parabolically varying $\Delta\omega_0$ map. After correcting for the fat blurring because of chemical shift $\Delta\omega_{cs}$, the effect of increasingly negative values of $\Delta\omega_0$ on the sharpness of contours between different tissues is well observable along the fatty ring structure, as it is subjected to different background off-resonance fields along the vertical axis. In some maps, isolated voxels show low matched T_1 and T_2 values, which means that for these voxels the dictionary did not contain a well-matching entry for the superposition of the MRF water and fat signal.

3.2 | Phantom validation

Figure 3 shows the validation of the MRF-Dixon sequence in the phantom. Figure 3A,B depict the parameter maps resulting from IR/MESE reference measurements, Cartesian MRF, standard (i.e., blurred) spiral MRF, and the proposed MRF-Dixon approach. While the phantom vials in the standard MRF maps exhibit fat blurring artefacts, these are greatly reduced in the MRF-Dixon maps. In Figure 3B, it can be seen that both spiral and the Cartesian MRF measurements underestimate the T_2 MESE values for large T_2 values. Figure 3C,D depict the mean values and SDs over the phantom vials for all 4 measurements. When comparing standard MRF to MRF-Dixon, it can be seen that blurred fat signal lowers the mean T_1 (T_2) values within those phantom vials that exhibit higher relaxation times than fat. Moreover, it results in large amounts of variation (i.e., high SDs). After deblurring, MRF-Dixon yields overall higher mean T_1 and T values than Cartesian MRF, which albeit are closer to the IR and MESE reference values. Figure 3E,F present the SDs separately. In the MRF-Dixon measurement, all STDs are reduced with respect to standard MRF for both T_1 and T_2, although Cartesian MRF and the IR/MESE reference sequences show even smaller SDs. Supporting Information Figure S3 depicts the NRMSEs calculated according to Equation 8, calculated per vial for T_1 and T_2. Not only with respect to the IR/MESE reference sequences, but also with respect to the Cartesian MRF sequence, the MRF-Dixon measurement yields smaller NRMSE values than the standard MRF measurement. This holds true for both T_1 and T_2. Average NRMSE values over

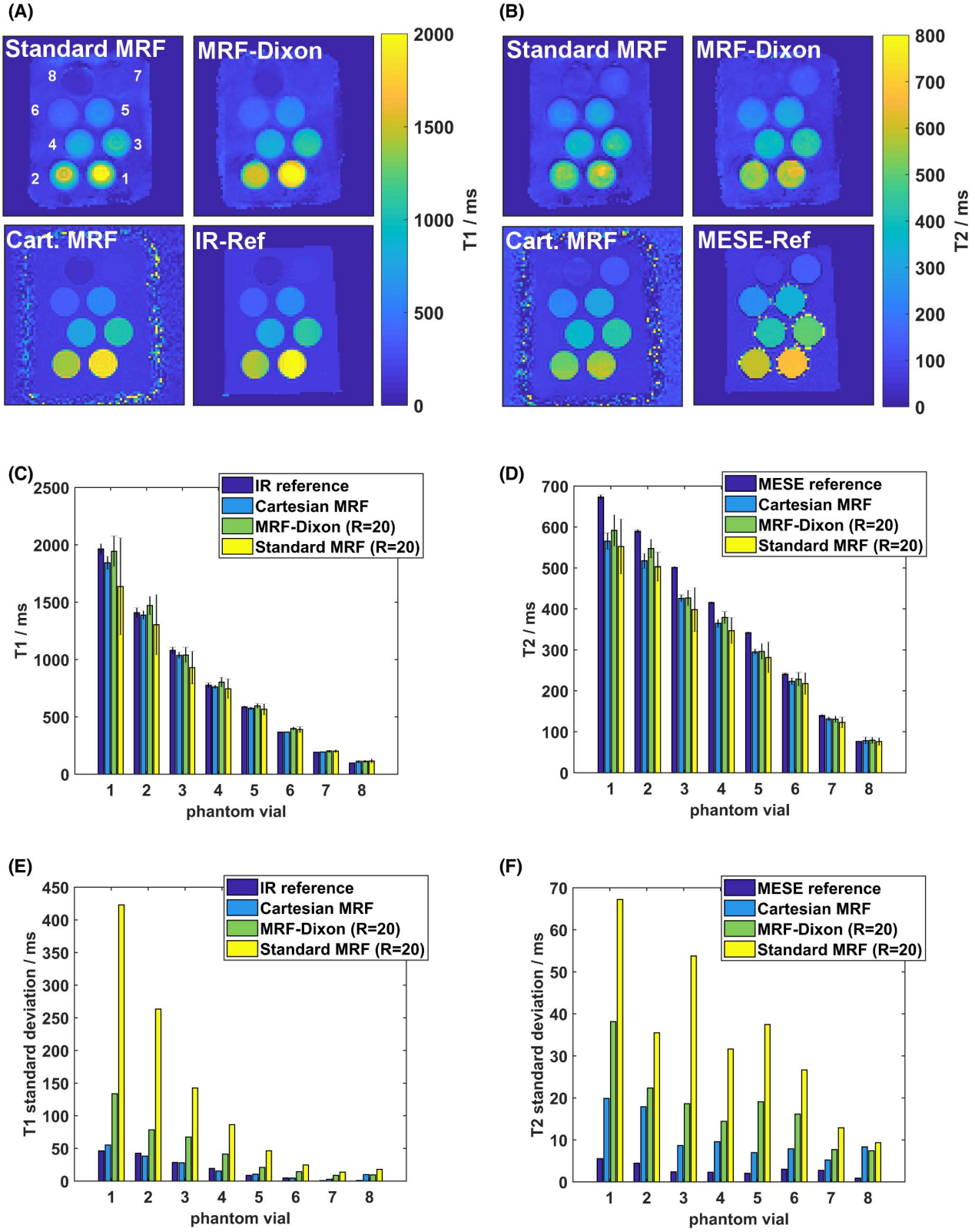

FIGURE 3 Validation of the MRF-Dixon sequence in a phantom. The phantom consists of 8 vials of gelatin mixed with different amounts of gadolinium embedded in lard. (A and B) T_1 and T_2 maps of the phantom measurements. Depicted are 100 × 100 voxel large zooms onto the phantom. Both spiral MRF measurements (i.e., the uncorrected standard MRF measurement and the blurring-corrected MRF-Dixon measurement) used an acceleration factor of $R = 20$. (C and D) Mean values and SDs of the T_1 and T_2 values in each phantom vial for the standard MRF measurement, the MRF-Dixon measurement, the Cartesian MRF measurement, and the IR reference measurement, respectively. (E and F) SDs only

the 8 phantom vials for T_1 are 16%, 8%, 15%, and 8% between standard MRF and IR reference, MRF-Dixon and IR reference, standard MRF and Cartesian MRF, and MRF-Dixon and Cartesian MRF, respectively. For T_2, corresponding values of 18%, 11%, 12%, and 7% are calculated.

3.3 | In vivo breast scans

As an example for the breast scans, we present the full data set for 1 volunteer. Further results are available in the Supporting Information Figures S4 and S5.

3.3.1 | Deblurring and water–fat separation

Figure 4 presents 2 maps of the background off-resonance $\Delta\omega_0$ of the main magnetic field. Figure 4A shows the mean off-resonance map ($\Delta\omega_0$-map) that we calculated from the MRF-Dixon measurement by using Equation 5 and a subsequent phase unwrapping step. Figure 4B shows the $\Delta\omega_0$-map as obtained from the Cartesian Dixon reference measurement. The mean $\Delta\omega_0$-map computed from the MRF-Dixon signals is free from phase wraps and does not show any artifacts from spiral sampling. In 1 spot that is marked by a white arrow, the 2 maps differ: the Cartesian Dixon reference map shows a local maximum, while the MRF-Dixon map does not. This discrepancy is also visible in the difference map in Figure 4C, which else shows differences between 0 and $-15 \cdot 2\pi$ rad/s in the breast area. This figure also reveals a more structured appearance of the MRF-Dixon map with respect to the (smoothed) Cartesian map.

Mean MRF signals (i.e., the temporal averages over the water–fat separated MRF trains) were calculated according to Equation 4. Figure 5A,D show the mean water and fat signal, respectively, before CPR deblurring. While the

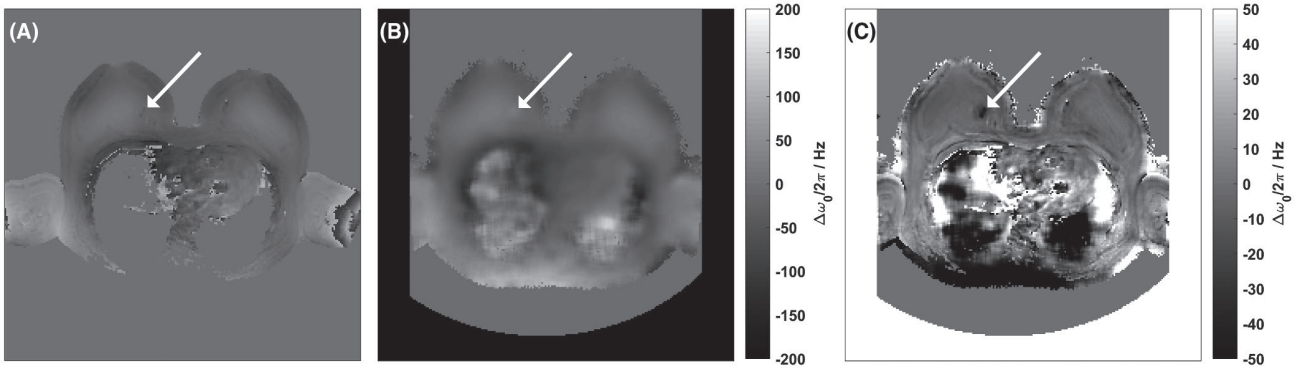

FIGURE 4 Off-resonance maps. (A) Mean off-resonance map as computed from the MRF-Dixon measurement according to Equation 5. (B) Off-resonance map as reconstructed by the scanner's 3-point Dixon sequence. The white arrow points out a location where (A) and (B) differ. (C) Difference map (i.e., B was subtracted from A)

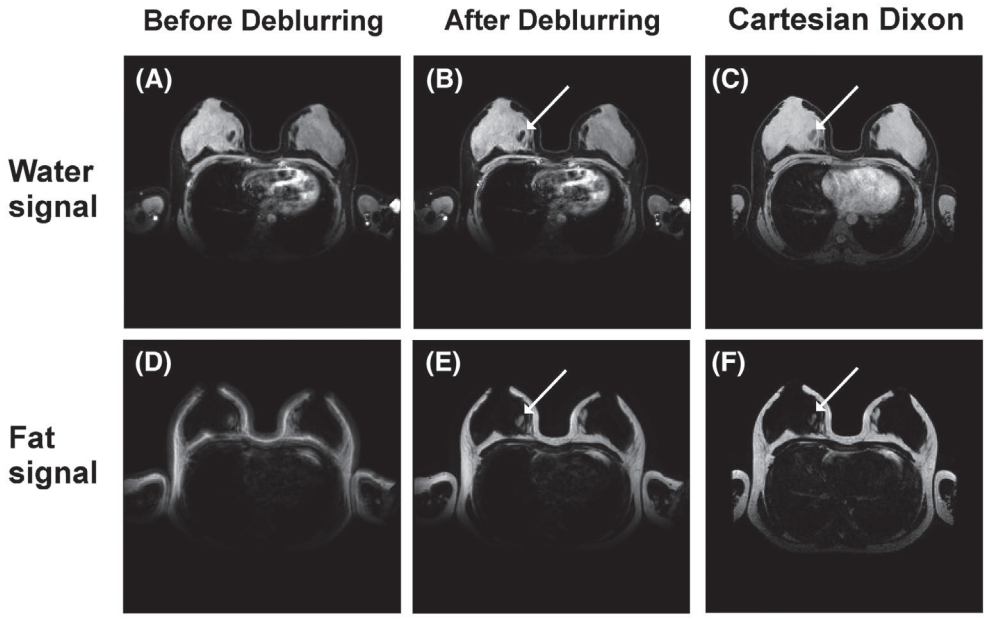

FIGURE 5 Deblurring results and comparison to the reference scan. (A) Mean MRF water signal and (D) mean MRF fat signal after Dixon water–fat separation, before CPR deblurring. (B) Mean MRF water signal and (E) mean MRF fat signal after Dixon water–fat separation, after CPR deblurring. (C) Cartesian 3-point Dixon water and (F) fat signal as obtained from the scanner reconstruction software

mean water signal shows little blurring, the mean fat signal is strongly smeared out. This makes the anatomic features hardly distinguishable. Figure 5B,E show the mean water and fat signal after CPR deblurring. Deblurring alters the mean fat signal most strongly, resulting in a fat distribution with sharp edges. The changes in the mean water signal because of deblurring are more subtle, but the deblurred mean water signal in Figure 5B reveals, for example, a sharper delineation of the skin. When comparing the deblurred images to the Cartesian Dixon water and fat image shown in Figure 5C,F, respectively, a close resemblance is observed: the same features are visible with a similar degree of sharpness. Yet, there is 1 visible difference between both measurements, namely in the same location that differed already in the $\Delta\omega_0$-maps. The local maximum in the Cartesian $\Delta\omega_0$-map results in a smaller fat signal and higher water signal in that location, which we indicated again by white arrows.

3.3.2 | Quantitative parameter maps

Figure 6 presents the results for the quantitative parameter maps. Figure 6A,B show the standard MRF matching to the first MRF train M_1, without any correction for spiral blurring. It is clearly visible that the fat blurring propagates into the T_1 and T_2 map. Specifically, areas of fatty tissue appear broadened and without any clear delineation to the adjacent fibroglandular tissue. This broadening also results in a breast size that is extending over the anatomical breast size. Furthermore, streak artifacts of circular shape are present in the T_2 maps. The T_1 and T_2 maps after deblurring are shown in Figure 6C,D for the undersampled MRF-Dixon measurement and in Figure 6E,F for the fully sampled MRF measurement, respectively. After CPR deblurring, the MRF matching yields improved parameter maps showing a sharp delineation between fibroglandular and fatty tissue. Fatty substructures within the breast are now clearly visible and the contour of the outer fat layer is no longer smeared out. When comparing the undersampled MRF-Dixon measurement to the fully sampled MRF-Dixon measurement, the T_1 and T_2 maps look very similar, indicating stability of our MRF-Dixon sequence to undersampling. However, the undersampled T_2 maps are generally noisier than their fully sampled counterparts. In the T_2 map in Figure 6D, a slightly streaky structure is visible also after deblurring. The T_2 map reconstructed from the fully sampled MRF-Dixon measurement is completely free of the aforementioned artifacts, as can be seen in Figure 6F. Because the MRF matching was corrected for the measured B_1^+, the reconstructed T_2 maps are free of asymmetry (i.e., they show similar T_2 values for the left and right breast). Figure 6G,H present the results of the T_1 and T_2 relaxometry measurements that we acquired for reference. Figure 6G shows the T_1 map as obtained from fitting Equation 6 to the IR measurements. Figure 6H shows the T_2 map as obtained from fitting Equation 7 to the MESE measurement. Both reference maps exhibit the same overall features as the parameter maps obtained by the MRF-Dixon method. However, the T_2 reference values of fatty tissue exhibit a positive offset with respect to the MRF-Dixon measurements. In addition, the T_1 reference values in fibroglandular tissue are overall smaller than the MRF-Dixon values.

To further assess the impact of fat blurring on small feature relaxometry, absolute difference maps between standard MRF measurement and MRF-Dixon measurement are shown in Figure 7A,C for T_1 and T_2, respectively. In both difference maps, a rim of altered T_1 and T_2 values is visible next to the fat border within the fibroglandular tissue. Within this zone, extending over ~4 pixels or ~7–8 mm, bias is added to the relaxation times and small features may be obscured. The line profiles depicted in Figure 7B,D show changes in FG tissue of ~300 ms for T_1 and ~30 ms for T_2. The fat blurring outside the breast yielding a larger apparent breast size is visible from the line profiles.

Results of the in vivo comparison between the proposed blurring correction by CPR and a center frequency correction can be found in Supporting Information Figure S6, presented exemplarily for 2 of the 6 volunteers.

4 | DISCUSSION AND CONCLUSIONS

This work addresses the blurring problem in spiral MRF for water and fat by a 3-point Dixon approach. Three fingerprint trains of different TEs permit both water–fat separation and deblurring without requiring a separate off-resonance map. Thereby, an accurate measurement of the relaxation times of small features by spiral MRF becomes possible in regions that are else compromised by the overlapping, blurred fat signal.

In the simulation study, we first investigated the bias of fat blurring on T_1 and T_2 of structures close to fatty tissue, depending on the spiral acquisition time. We showed that for $T_{acq} = 7$ ms, which was also used for the subsequent measurements, fat blurring is expected to lead to an incorrect quantification of the relaxation times within a region of ~7–8 mm width next to fatty structures. Further simulations including background off-resonance blurring of different strengths underlined the additional benefit of CPR (i.e., correction of both fat blurring and off-resonance blurring) over executing a center frequency correction of the fat signal alone.

In the phantom validation experiments, the proposed deblurring approach reduced the SDs in all phantom vials in comparison to standard MRF. The remaining difference to the even smaller SDs of the reference methods may be attributable to small amounts of residual blurred signal, which may also explain the unexpected discrepancies in mean

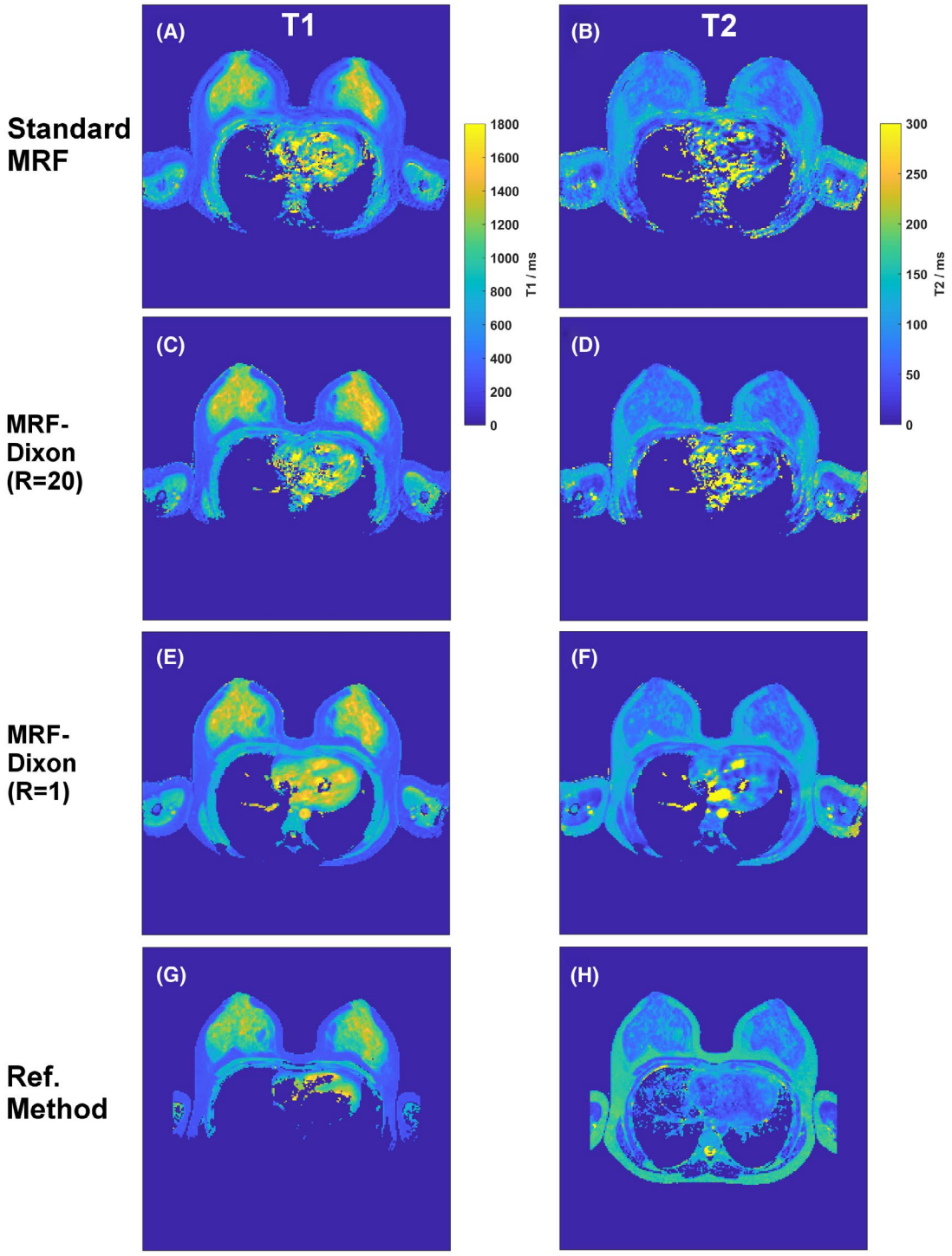

FIGURE 6 Relaxation time maps. (A and B) Blurry T_1 and T_2 map as obtained from the standard MRF approach (i.e., when matching only the first out of the 3 MRF trains to the dictionary). (C and D) Deblurred T_1 and T_2 map as obtained from the undersampled (R = 20) MRF-Dixon measurement. (E and F) Deblurred T_1 and T_2 map as obtained from the fully sampled (R = 1) MRF-Dixon measurement. (G and H) T_1 and T_2 map as obtained from the reference methods (i.e., the inversion recovery and MESE measurement)

values between MRF-Dixon and Cartesian MRF. It should be noted, however, that a mean value alone does not always permit to evaluate the amount fat blurring, because the blurred fat signal results in an areas of under- as well as of overestimated relaxation times within the vials. We observed smaller NRMSE values between MRF-Dixon and Cartesian reference relaxation times than between standard MRF and the reference. We equally see this improvement when calculating the NRMSEs with respect to Cartesian MRF. It should be underlined that the latter comparison judges the effect of

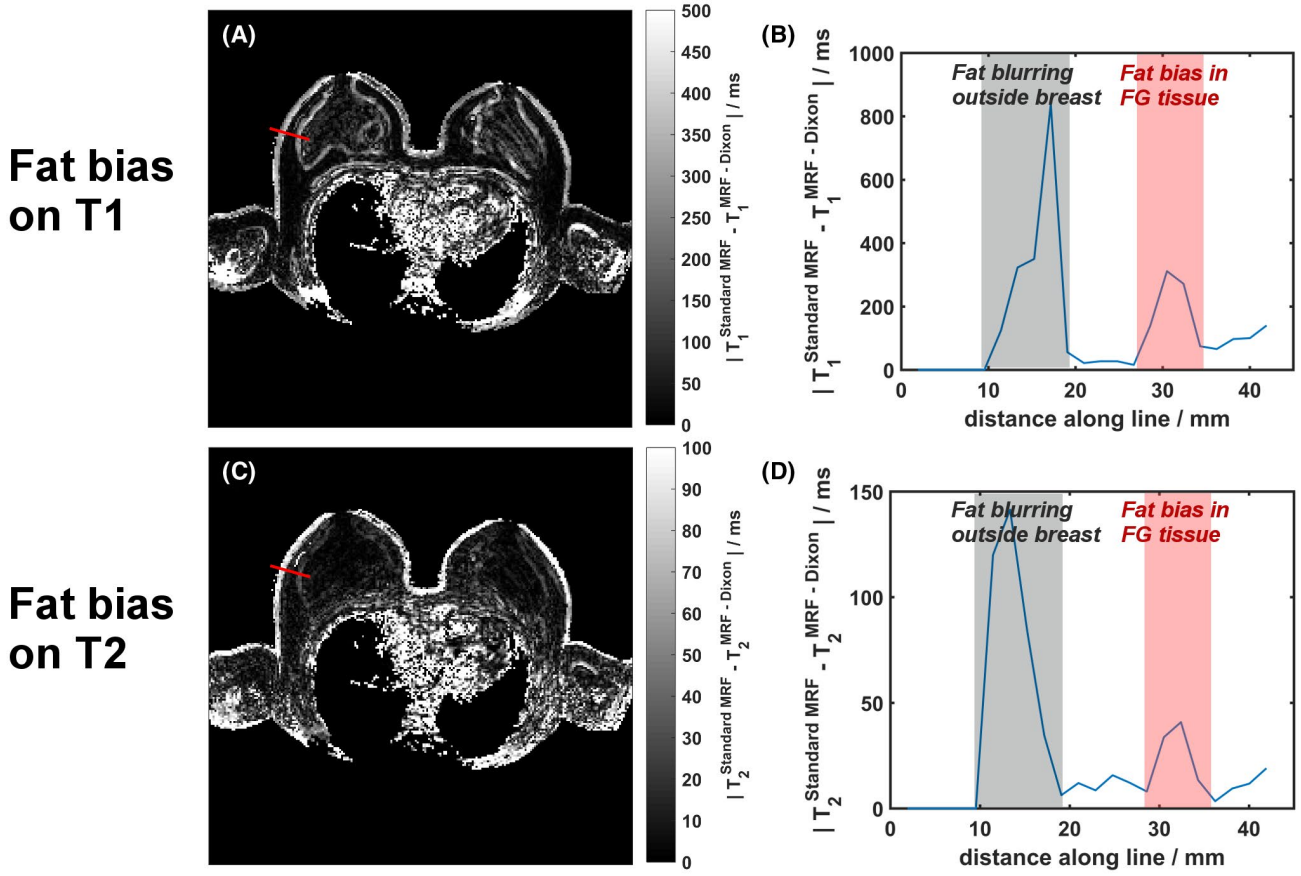

FIGURE 7 (A) Absolute T_1 difference map between the (blurry) standard MRF measurement and the (deblurred) MRF-Dixon measurement. The fat blurring manifests as a rim around the fatty structures. (B) Absolute T_1 difference profile along the red line marked in (A). (C) Absolute T_2 difference map between the standard MRF measurement and the MRF-Dixon measurement. (D) Absolute T_1 difference profile along the red line marked in (C). It is visible from the profiles that fat blurring causes bias within the fibroglandular tissue along a distance of ~4 pixels (i.e., ~7–8 mm)

our blurring correction best, because the spiral and Cartesian MRF sequences were using equal acquisition parameters apart from the signal readout. The difference in long T_2 values between MRF and MESE measurements is likely attributable to increased diffusion effects in the MRF sequence.[36] However, we do not expect such large T_2 in breast tissues.[37] We therefore conclude that the validation of the MRF sequence was relevant with respect to the intended application.

For the in vivo breast scans, the deblurring approach via CPR resulted in blurring-free mean water and fat signals. The effect of deblurring was most prominent for the fat signal, because the scanner's resonance frequency usually adjusts close to the water resonance frequency. Retrospectively, the successful deblurring justifies using the mean off-resonance map during CPR, despite minor differences to the Cartesian Dixon map. The discrepancy is likely because of the smoothness constraint used in the computation of the Cartesian Dixon map and needs further investigation. In this work, we applied water–fat separation and CPR sequentially. Although the measured off-resonance maps were found to vary smoothly within the breast, a joint method may provide improved deblurring if $\Delta\omega_0$ undergoes rapid changes.[38] Further improvements on CPR itself are reported, concerning (e.g., accelerated reconstruction times[39-41]) simultaneous correction for concomitant gradient fields,[41] autofocusing techniques,[42] or the application to rapidly varying off-resonance distributions.[43]

Deblurring by CPR further permitted an improved feature delineation in both the T_1 and the T_2 maps. The quantitative maps of the undersampled MRF-Dixon measurement agreed well with those of the fully sampled one, despite the 20-fold acceleration. Next to the phantom measurements, this is an important indicator for the stability of our MRF-Dixon sequence in the presence of undersampling. We suggest that such a comparison should be made each time that an MRF sequence is changed, especially if the amount of acquired information is decreased (e.g. when reducing the number of TR intervals or the voxel sizes).

Future effort will comprise removal of the streak artifacts, which are supposedly because of wrong registration of signal in the presence of heart movement and through-plane blood

flow. While for Cartesian sampling the in-flowing blood results in coherent ghosts along the phase-encoding direction,[44] the spiral readout, bearing a continuously changing phase-encoding direction, smears such signal around the source of flow in a spiral-looking manner. A solution to this problem might lie in presaturation of signal in the heart region. A different strategy may be to increase the SNR (and therefore to decrease the importance of flow artifacts) during reconstruction, such as by compressed sensing[45] or matrix completion methods.[46]

Respiratory motion was not included into reconstruction of the in vivo MRF scans, but it was minimized by tightly fixing the breast between 2 fixation paddles along the feet–head direction. In this setting, we did not observe motion artifacts. Including motion correction into reconstruction is, however, an interesting topic for future research. Several works consider motion correction for MRF,[47-49] but are currently limited to rigid motion.

We corrected the presented MRF-Dixon measurements for in plane B_1^+ inhomogeneity. Slice profile effects were not corrected during MRF matching; however, we used an RF pulse shape with a time-bandwidth product of 10.2 that minimizes slice profile effects. B_1^+ correction proved to remove the large intra-breast inhomogeneity of the T_2 values.[50] MRF is known to be prone to B_1^+ inhomogeneity,[51] because the dictionary reconstruction relies on exact knowledge of the flip angle train. Admittedly, a faster B_1^+ mapping method would be preferred for future MRF exams.

In vivo, differences were present between the relaxation times in the MRF and the reference maps. The MRF and reference pulse sequences differed in the used gradients and RF pulse shapes, which complicates their direct comparison. Slice profile effects and imperfect inversion pulses,[52-54] diffusion,[36,55] and magnetization transfer effects[56,57] are confounding factors affecting both MRF and reference relaxation measurements to different degrees, which can explain the differences in the relaxation time maps. In addition, fat has multiple spectral components with different relaxation times. This may lead to different apparent relaxation times for different sequences. These discrepancies are a problem yet to be solved by qMRI, which we cannot remedy by our deblurring approach alone.

Three separate MRF trains of different echo time are demonstrated here as a proof of principle that the approach works. Although we were still able to acquire a single slice in <1 min, prolonged scan times will be of concern for volumetric acquisitions which are of relevance for breast imaging. Acceleration can be achieved by performing only a 2-point Dixon water–fat separation with an additional phase-unwrapping step.[58] Instead of acquiring 2 or 3 separate MRF trains, several spirals may be acquired in 1 TR interval. For multiple slices, the delay times between MRF trains can moreover be used to acquire another slice. It should be mentioned that MRF in the breast with fat suppression as proposed by Chen et al[7] is advantageous with respect to scan time, as only 1 MRF train is needed. A different strategy for water–fat separation without the need for several echo trains can lie in dictionary-based methods,[27] which may afterward be combined with spiral deblurring.

Deblurring of MRF data was demonstrated for 6 young healthy volunteers, presenting different breast densities. Blurring was removed both in case of demarcated fibroglandular–fat interfaces and for more distributed mixtures of fibroglandular and fatty tissue. Because of the technical feasibility nature of the study, the measurements do not reflect overall demography and ACR distribution in women. However, our maps already suggests that there may be a high variability in breast T_1 values—partially caused by partial volume effects where fat and water are present in the same voxel, but also especially within areas of fibroglandular tissue only, where most breast carcinoma can be found. This challenges tissue quantification in the breast.

Finally, we would like to point out that the separated water and fat MRF data may be used to compute the fat signal fraction per voxel, either from the water and fat proton densities or by using the mean water and fat signals. Because this would add 1 more diagnostic parameter to the outcome of MRF, we aim to compare and validate these approaches in a future study.

ACKNOWLEDGMENTS

This project has received funding from the European Union's Horizon 2020 research and innovation program under the Marie Skłodowska-Curie grant agreement 642445 and under grant agreement 667211.

CONFLICT OF INTEREST

Mariya Doneva, Peter Koken, and Aaldert Elevelt are currently employed by Philips Research Europe.

ORCID


Teresa Nolte https://orcid.org/0000-0003-3167-7121

REFERENCES

1. Tofts P. *Quantitative MRI of the brain: measuring changes caused by disease*. Chichester: John Wiley & Sons Ltd; 2005:650.
2. Cheng HM, Stikov N, Ghugre NR, Wright GA. Practical medical applications of quantitative MR relaxometry. *J Magn Reson Imaging*. 2012;36:805–824.
3. Neeb H, Boer A, Gliedstein D, Raspe M, Schenk J. Predicting multiple sclerosis from normal appearing brain matter - combination of quantitative MRI metrics with supervised learning. In *Proceedings of the World Congress on Engineering and Computer Science*, San Francisco, CA, 2014. Vol I.

4. Liu L, Yin B, Deng GY, Lu YP, Peng WJ. Changes of T2 relaxation time from neoadjuvant chemotherapy in breast cancer lesions. *Iran J Radiol*. 2016;13:e24014.
5. Tan PC, Pickles MD, Lowry M, Manton DJ, Turnbull LW. Lesion T2 relaxation times and volumes predict the response of malignant breast lesions to neoadjuvant chemotherapy. *Magn Reson Imaging*. 2008;26:26–34.
6. Manton DJ, Chaturvedi A, Hubbard A, et al. Neoadjuvant chemotherapy in breast cancer: early response prediction with quantitative MR imaging and spectroscopy. *Br J Cancer*. 2006;94:427–435.
7. Chen Y, Panda A, Pahwa S, et al. Three-dimensional MR fingerprinting for quantitative breast imaging. *Radiology*. 2019;290:33–40.
8. Seo M, Ryu JK, Jahng G-H, et al. Estimation of T2* relaxation time of breast cancer: correlation with clinical, imaging and pathological features. *Korean J Radiol*. 2017;18:238–248.
9. Liu LI, Yin BO, Shek K, et al. Role of quantitative analysis of T2 relaxation time in differentiating benign from malignant breast lesions. *J Int Med Res*. 2018;46:1928–1935.
10. Ma D, Gulani V, Seiberlich N, et al. Magnetic resonance fingerprinting. *Nature*. 2013;495:187–193.
11. Jiang Y, Ma D, Seiberlich N, Gulani V, Griswold MA. MR fingerprinting using fast imaging with steady state precession (FISP) with spiral readout. *Magn Reson Med*. 2015;74:1621–1631.
12. Körzdörfer G, Pfeuffer J, Kluge T, et al. Effect of spiral undersampling patterns on FISP MRF parameter maps. *Magn Reson Imaging*. 2019;62:174–180.
13. Kara D, Fan M, Hamilton J, Griswold M, Seiberlich N, Brown R. Parameter map error due to normal noise and aliasing artifacts in MR fingerprinting. *Magn Reson Med*. 2019;81:3108–3123.
14. Block KT, Frahm J. Spiral imaging: a critical appraisal. *J Magn Reson Imaging*. 2005;21:657–668.
15. Ma J. Dixon techniques for water and fat imaging. *J Magn Reson Imaging*. 2008;28:543–558.
16. Boernert P, Schomberg H, Aldefeld B, Groen J. Improvements in spiral MR imaging. *MAGMA*. 1999;9:29–41.
17. Lin C, Rogers C, Majidi SS. Fat suppression techniques in breast magnetic resonance imaging: a critical comparison and state of the art. *Rep Med Imaging*. 2015;8:37–49.
18. Sridaran S, Panda A, Chen Y, et al. Normative T1 and T2 relaxation times and measurement repeatability of abdomen organs at 3T using 2D MR fingerprinting. In *Proceedings of the 26th Annual Meeting of ISMRM*, Paris, France, 2018. Abstract 4253.
19. Kuhl CK, Klaschik S, Mielcarek P, Gieseke J, Wardelmann E, Schild HH. Do T2-weighted pulse sequences help with the differential diagnosis of enhancing lesions in dynamic breast MRI? *J Magn Reson Imaging*. 1999;9:187–196.
20. Dixon WT. Simple proton spectroscopic imaging. *Radiology*. 1984;153:189–194.
21. Boernert P, Koken P, Eggers H. Spiral water–fat imaging with integrated off-resonance correction on a clinical scanner. *J Magn Reson Imaging*. 2010;32:1262–1267.
22. Ostenson J, Robison RK, Zwart NR, Welch EB. Multifrequency interpolation in spiral magnetic resonance fingerprinting for correction of off-resonance blurring. *Magn Reson Imaging*. 2017;41:63–72.
23. Koken P, Amthor T, Doneva M, et al. Improving accuracy in MR fingerprinting by off-resonance deblurring. In Proceedings of the 25th Annual Meeting of ISMRM, Honolulu, HI, 2017. Abstract 5067.
24. Koolstra K, Webb A, Koken P, Nehrke K, Börnert P. Water-fat separation in spiral magnetic resonance fingerprinting using conjugate phase reconstruction. In Proceedings of the 26th Annual Meeting of ISMRM, Paris, France, 2018. Abstract 0681.
25. Nolte T, Truhn D, Gross-Weege N, et al. Undersampled spiral magnetic resonance fingerprinting with water and fat blurring correction. In Proceedings of the 25th Annual Meeting of ISMRM, Paris, France, 2018. Abstract 4215.
26. Ostenson J, Damon BM, Welch EB. MR fingerprinting with simultaneous T1, T2, and fat signal fraction estimation with integrated B0 correction reduces bias in water T1 and T2 estimates. *Magn Reson Imaging*. 2019;60:7–19.
27. Cencini M, Biagi L, Kaggie JD, Schulte RF, Tosetti L, Buonincontri G. Magnetic resonance fingerprinting with dictionary-based fat and water separation (DBFW MRF): a multi-component approach. *Magn Reson Med*. 2019;81:3032–3045.
28. King KF. Gridding reconstruction. In: Bernstein MA, King KF, Zhou XJ, eds. *Handbook of MRI pulse sequences*. Burlington: Elsevier Academic Press; 2004:506–521.
29. Ahunbay E, Pipe JG. Rapid method for deblurring spiral MR images. *Magn Reson Med*. 2000;44:491–494.
30. Man L, Pauly JM, Macovski A. Multifrequency interpolation for fast off-resonance correction. *Magn Reson Med*. 1997;37:785–792.
31. Zhao BO, Haldar JP, Liao C, et al. Optimal experiment design for magnetic resonance fingerprinting: Cramér-Rao bound meets spin dynamics. *IEEE Trans Med Imaging*. 2019;38:844–861.
32. Scheffler K. A pictorial description of steady-states in rapid magnetic resonance imaging. *Concepts Magn Reson*. 1999;11:291–304.
33. Sommer K, Amthor T, Koken P, Meineke J, Doneva M. Determination of the optimum pattern length of MRF sequences. In *Proceedings of the 25th Annual Meeting of ISMRM*, Honolulu, HI, 2017. Abstract 1491.
34. Yarnykh VL. Actual flip-angle imaging in the pulsed steady state: a method for rapid three-dimensional mapping of the transmitted radiofrequency field. *Magn Reson Med*. 2007;57:192–200.
35. Reeder SB, Wen Z, Yu H, et al. Multicoil dixon chemical species separation with an iterative least-squares estimation method. *Magn Reson Med*. 2004;51:35–45.
36. Kobayashi Y, Terada Y. Diffusion-weighting caused by spoiler gradients in the fast imaging with steady-state precession sequence may lead to inaccurate T2 measurements in MR fingerprinting. *Magn Reson Med Sci*. 2019;18:96–104.
37. Edden R, Smith SA, Barker PB. Longitudinal and multi-echo transverse relaxation times of normal breast tissue at 3 Tesla. *J Magn Reson Imaging*. 2010;32:982–987.
38. Wang D, Zwart NR, Pipe JG. Joint water–fat separation and deblurring for spiral imaging. *Magn Reson Med*. 2018;79:3218–3228.
39. Noll DC, Fessler JA, Sutton BP. Conjugate phase MRI reconstruction with spatially variant sample density correction. *IEEE Trans Med Imaging*. 2005;24:325–336.
40. Moriguchi H, Dale BM, Lewin JS, Duerk JL. Block regional off-resonance correction (BRORC): a fast and effective deblurring method for spiral imaging. *Magn Reson Med*. 2003;50:643–648.
41. Chen W, Sica CT, Meyer CH. Fast conjugate phase image reconstruction based on a Chebyshev approximation to correct for B0 field inhomogeneity and concomitant gradients. *Magn Reson Med*. 2008;60:1104–1111.
42. Smith TB, Nayak KS. Automatic off-resonance correction in spiral imaging with piecewise linear autofocus. *Magn Reson Med*. 2013;69:82–90.

43. Makhijani MK, Nayak KS. Exact correction of sharply varying off-resonance effects in spiral MRI. In *Proceedings of 3rd IEEE International Symposium on Biomedical Imaging: Nano to Macro*, Arlington, VA, 2006. p. 730–733.
44. Li Z, Hu HH, Miller JH, et al. A spiral spin-echo mr imaging technique for improved flow artifact suppression in T1-weighted postcontrast brain imaging: a comparison with Cartesian turbo spin-echo. *AJNR Am J Neuroradiol*. 2016;37:642–647.
45. Lustig M, Donoho DL, Santos JM, Pauly JM. Compressed sensing MRI. *IEEE Signal Process Mag*. 2008;25:72–82.
46. Doneva M, Amthor T, Koken P, Sommer K, Börnert P. Matrix completion-based reconstruction for undersampled magnetic resonance fingerprinting data. *J Magn Reson Imaging*. 2017;41:41–52.
47. Mehta BB, Ma D, Pierre EY, Jiang Y, Coppo S, Griswold MA. Image reconstruction algorithm for motion insensitive MR fingerprinting (MRF): MORF. *Magn Reson Med*. 2018;80:2485–2500.
48. Cruz G, Jaubert O, Schneider T, Botnar RM, Prieto C. Rigid motion-corrected magnetic resonance fingerprinting. *Magn Reson Med*. 2019;81:947–961.
49. Yu Z, Zhao T, Assländer J, Lattanzia R, Sodickson DK, Cloos MA. Exploring the sensitivity of magnetic resonance fingerprinting to motion. *Magn Reson Imaging*. 2018;54:241–248.
50. Winkler SA, Rutt BK. Practical methods for improving B_1^+ homogeneity in 3 Tesla breast imaging. *J Magn Reson Imaging*. 2015;41:992–999.
51. Buonincontri G, Schulte RF, Cosottini M, Tosetti M. Spiral MR fingerprinting at 7 T with simultaneous B1 estimation. *J Magn Reson Imaging*. 2017;41:1–6.
52. Ben-Eliezer N, Sodickson DK, Block KT. Rapid and accurate T2 mapping from multi–spin-echo data using bloch-simulation-based reconstruction. *Magn Reson Med*. 2015;73:809–817.
53. Lebel RM, Wilman AH. Transverse relaxometry with stimulated echo compensation. *Magn Reson Med*. 2010;64:1005–1014.
54. Kingsley PB, Ogg RJ, Reddick WE, Steen RG. Correction of errors caused by imperfect inversion pulses in MR imaging measurement of T1 relaxation times. *Magn Reson Imaging*. 1998;16:1049–1055.
55. Weigel M, Hennig J. Diffusion sensitivity of turbo spin echo sequences. *Magn Reson Med*. 2012;67:1528–1537.
56. Malik SJ, Teixeira R, Hajnal JV. Extended phase graph formalism for systems with magnetization transfer and exchange. *Magn Reson Med*. 2018;80:767–779.
57. Prantner AM, Bretthorst GL, Neil JJ, Garbow JR, Ackerman J. Magnetization transfer induced biexponential longitudinal relaxation. *Magn Reson Med*. 2008;60:555–563.
58. Coombs BD, Szumowski J, Coshow W. Two-point dixon technique for water-fat signal decomposition with B0 inhomogeneity correction. *Magn Reson Med*. 1997;38:084–889.

SUPPORTING INFORMATION

Additional supporting information may be found online in the Supporting Information section at the end of the article.

FIGURE S1 More simulations were conducted to evaluate the combined effect of fat blurring because of $\Delta\omega_{cs}$ and of the background off-resonance field $\Delta\omega_0$ at a fixed spiral acquisition time of $T_{acq} = 7$ ms. (A and B) Line profiles through the test structure (TS) for different constant background off-resonance frequencies $\Delta\omega_0$ and fat blurring $\Delta\omega_{cs}$ within the fatty tissue. (C and D) Corresponding mean values and SDs of T_1 and T_2 within the TS. (E and F) Line profiles through the test structure (TS) for different constant $\Delta\omega_0$ and $\Delta\omega_{cs}$ set to 0 (i.e., after a center frequency correction for $\Delta\omega_{cs}$ has been applied to the fatty tissue). (G and H) Corresponding mean values and SDs of T_1 and T_2 within the TS

FIGURE S2 Simulations with spatially varying off-resonance maps, using (A) a linearly varying $\Delta\omega_0$ map and (B) a parabolically varying $\Delta\omega_0$ map. The fatty ring structure therefore experiences locally different strengths of $\Delta\omega_0$ along the vertical axis. The spiral acquisition time was fixed to 7 ms for all simulations. The T_1 and T_2 maps in the left column show the combined effect of off-resonance blurring and fat blurring because of chemical shift on the fatty ring structure (i.e., $\Delta\omega = \Delta\omega_0 + \Delta\omega_{cs}$). The T_1 and T_2 maps in the right column show the effect of off-resonance blurring alone (i.e., $\Delta\omega_{cs}$ was set to 0). The latter scenario corresponds to a center frequency correction of the blurred image (i.e., correcting only for the fat blurring because of chemical shift)

FIGURE S3 Validation of the MRF-Dixon sequence in a phantom, NRMSE calculations. (A) T_1-NRMSE between standard MRF/MRF-Dixon and IR reference measurement. (B) T_1-NRMSE between standard MRF/MRF-Dixon and the Cartesian MRF measurement. (C) T_2-NRMSE between standard MRF/MRF-Dixon and MESE reference measurement. (D) T_2-NRMSE between standard MRF/MRF-Dixon and the Cartesian MRF measurement

FIGURE S4 Deblurring and water–fat separation results for volunteers 1, 2, 3, 5, and 6. The first column shows the mean water and fat signal as obtained from the MRF-Dixon measurements without deblurring. The second column shows the mean water and fat signal as obtained from the MRF-Dixon after deblurring. The third column shows the water and fat signal as obtained by the Cartesian Dixon reference measurement

FIGURE S5 Relaxation time maps for volunteers 1, 2, 3, 5, and 6. Top row: T_1 and T_2 map as obtained from the standard MRF matching to 1 single MRF train (i.e., without deblurring). Second (and third) row: T_1 and T_2 map as obtained from the undersampled (and the fully sampled, if acquired) MRF-Dixon measurement after deblurring. The fully sampled measurement was not acquired for volunteers 1, 3, and 6 because of the long total scan time. Bottom row: T_1 and T_2 map as obtained from the reference methods (i.e., inversion recovery for T_1 and multi-echo spin echo for T_2)

FIGURE S6 In vivo comparison of CPR (i.e., correction for both background off-resonance and fat chemical shift blurring) and center frequency (CF) correction (i.e., correction of fat chemical shift blurring only). The comparison is shown exemplarily for the undersampled MRF-Dixon data sets of

(A) volunteer 4 and (B) volunteer 5, the latter 1 presenting areas of stronger background off-resonance than the first 1. Top left: off-resonance map. Top right: absolute difference between the mean deblurred fat signals. Bottom left: difference between the MRF T_1 maps. Bottom right: difference between the MRF T_2 maps. For the difference plots, the results obtained by CPR were subtracted from the results obtained by center frequency correction only. For both volunteers, some differences in the mean fat signal become apparent near the FG-fatty tissue interfaces. Slight differences in the MRF T_1 and T_2 maps are visible in the corresponding locations

How to cite this article: Nolte T, Gross-Weege N, Doneva M, et al. Spiral blurring correction with water–fat separation for magnetic resonance fingerprinting in the breast. *Magn Reson Med*. 2020;83:1192–1207. https://doi.org/10.1002/mrm.27994